

## Article

# Seismic Response Analysis of Anchor Joint in Shield-Driven Tunnel Considering Soil-Structure Interaction

Gaole Zhang<sup>1</sup>, Wenjun Zhang<sup>1,2,\*</sup>, Jianbing Qi<sup>1</sup>, Rongjian Niu<sup>1</sup> and Chi Zhang<sup>1</sup>

<sup>1</sup> School of Civil Engineering, Tianjin University, Tianjin 300350, China; zhanggaole100@tju.edu.cn (G.Z.); qi\_jianbing123@tju.edu.cn (J.Q.); rigel07@tju.edu.cn (R.N.); carezhang@tju.edu.cn (C.Z.)

<sup>2</sup> School of Civil Engineering and Architecture, Guangxi University, Nanning 530004, China

\* Correspondence: wjzhang@tju.edu.cn

**Abstract:** The seismic behavior of the anchor joint in shield-driven tunnel is very difficult to determine with the conventional methods due to the extensive simplifications. This paper proposed an improved approach to investigate the seismic response of the anchor joint, considering both the soil-structure-interaction effect and the actual geometric features. Two three-dimensional numerical models were established, including the soil-tunnel system and the refined model of the anchor joint. A seismic analysis study was first conducted on the soil-tunnel model under different seismic input waves to obtain the responses of the joint opening and offset. Then, these results were imposed on the refined model of anchor joint to further examine its detailed performance under seismic excitations. The joint opening and offset under earthquake excitations from different directions were discussed. The distribution characteristics of the stress of the anchor joint were interpreted. Finally, safety evaluations on the anchor joint were executed based on the overall seismic responses. The results show that the maximum opening and offset of the anchor joint under the two-directional horizontal earthquake are greater than those under the unidirectional conditions, while different deformation trends are observed for the joints at distinct locations. The maximum opening of the anchor joint can reach 0.73 mm, whereas the peak offset is only 0.35 mm. The local plastic strain of the anchor joint increases under the seismic action, but all of the joints are still kept in the safe state under the most unfavorable conditions. The developed method in this paper can also be accessed by the seismic study on other types of joints with complex structural components in shield tunnels.

**Keywords:** shield tunnel; anchor joint; seismic response; numerical analysis; soil-structure interaction



**Citation:** Zhang, G.; Zhang, W.; Qi, J.; Niu, R.; Zhang, C. Seismic Response Analysis of Anchor Joint in Shield-Driven Tunnel Considering Soil-Structure Interaction. *Appl. Sci.* **2022**, *12*, 6362. <https://doi.org/10.3390/app12136362>

Academic Editor: Marco Vona

Received: 1 June 2022

Accepted: 20 June 2022

Published: 22 June 2022

**Publisher's Note:** MDPI stays neutral with regard to jurisdictional claims in published maps and institutional affiliations.



**Copyright:** © 2022 by the authors. Licensee MDPI, Basel, Switzerland. This article is an open access article distributed under the terms and conditions of the Creative Commons Attribution (CC BY) license (<https://creativecommons.org/licenses/by/4.0/>).

## 1. Introduction

Shield-driven tunnel has been widely used for the construction of urban underground transportation in the past few decades, and a great number of studies have been conducted to obtain a better knowledge of the mechanical and waterproof performance of segmental lining structures under the static and seismic action [1–5]. According to the published investigations [6,7], tunnels are vulnerable to damage under earthquake motions, especially for the joint area, which has been repeatedly proven to be the weak component in the whole tunnel. It should be noted that if the damage near the joint develops into obvious cracks, more secondary disasters may happen, including water leakage, sand gushing, and even collapse. Thus, it is of great importance to study the seismic response of the segmental joint in shield tunnels.

Generally, the seismic loading should be regarded as a key control factor during the design of a shield tunnel in earthquake-prone areas [8]. To capture the seismic performance of the shield tunnel, quite a few methods have been proposed and adopted. The free-field deformation approach is commonly used in earlier research [9], which neglects the soil-structure interaction (SSI). Using this method, the parameters for executing calculations are easy to gain, whereas inaccurate results may be obtained due to its excessive simplification.

It is well known that the SSI effect has a significant influence on the static and dynamic response of the structures [10–12]. Thus, the SSI effect should be properly taken into account to obtain satisfactory results. In this concern, Brachman et al. [13] conducted full-scale tests to study the effectiveness of conventional orthotropic shell theory in soil-structure interaction analyses. Abdel-Sayed and Salib [14] investigated the possible soil failures caused by centric live loads based on a finite element method considering the SSI effect. Yeau et al. [15] discussed the parameters which may have a great influence on the performance of the in-service culverts, including cover depth, size, and load application. Kasper and Meschke [16] examined the SSI effect on the shield tunneling process from the aspects of grout material properties and soil cover depth. Maleska and Beben [17] established an improved numerical model to explore the impact of soil cover depth on the behavior of soil-steel composite bridges during an earthquake. Maleska et al. [18] carried out a response analysis to reveal the behavior of the soil-steel composite tunnels under seismic excitations. Kuribayashi et al. [19] set up a beam-spring system to determine the longitudinal seismic behavior of the shield tunnel, in which the tunnel can be simulated as the beam, while the SSI effect can be considered through adding springs in different directions. Given that the beam element cannot totally represent the three-dimensional (3D) structural characteristics of the tunnel, more advanced methods were further presented through replacing the beam with cylindrical shells [20–22]. The analytical methods mentioned above provide valuable insights into the seismic response of shield tunnels, while it is insufficient to fully reveal the seismic characteristics of the segmental linings and joints owing to the inevitable extreme assumptions during derivation of the equations. Conducting experiments (e.g., shaking table tests and centrifuge tests) is another effective way [23,24], in which the tunnel model can be manufactured with more local details such as the bolts, gaskets, longitudinal and circumferential joints. Wang et al. [25] carried out shaking table tests to identify the consecutive damage of the tunnel linings, and the test phenomena were compared with those observed in field exploration. Wang et al. [26] examined the dynamic properties of two shallow-buried tunnels. From their findings, there are great differences in the responses of displacement and acceleration of the two different tunnels. Additionally, the numerical method has also gained wide adoption because of its advantages of cost-effectiveness, and flexible behavior in modeling the refined or simplified structures [27–29].

As the shield tunnel is a prefabricated structure consisting of numerous segments connected by joints, its mechanical behavior is highly different from those constructed with in-situ casting. There are many available publications about the weakened effect of the joint under static action [30–32], while that under seismic action is in need of further study. For this purpose, Zhang et al. [33] established a 3D finite element model (FEM) to analyze the dynamic characteristics of different types of bolt joints in shield tunnels. Liu et al. [34] studied the strength degradation, hysteresis behavior, energy dissipation, and the failure modes of the joints between prefabricated segments and cast-in-site structures under conditions of several earthquake excitations. Yang et al. [35] checked the distribution features of the joint opening on the basis of a FEM under multidirectional input waves to grasp the impact of seismic loading. Yan et al. [36] obtained the contact pressure, opening, and offset of the joint in a shield tunnel subjected to seismic loading so that the waterproof behavior of the joint can be considered under such conditions.

Overall, the research mentioned above has made great contributions to the comprehensive understanding of the seismic response of the segmental joint. However, the existing studies only cover the conventional bolt joints, while there are few reports on the seismic performance of the newly developed joints with a more complicated structural system, such as the anchor joint, FRP-Key joint, and CT joint [37–39]. These new joints have the characteristics of great strength, high precision, and quick connection [40], which will be the main trend of shield tunneling. Therefore, it is critical to conduct seismic response analysis of these new types of joints. Nevertheless, there are great challenges to directly reflecting the complex geometric features of the new joints during the dynamic numerical simulation, which may lead to too much increase in degrees of freedom to obtain computa-

tional convergence. On the other hand, neglecting the local details of the new joints may result in an unexpected negative influence on the final seismic response. Consequently, it is essential to propose more advanced methods for the seismic analysis of the new joints so that a good balance can be reached between the reliability and implementation difficulty.

This paper aims at investigating the seismic response of the anchor joint in shield tunnels considering soil-structure interaction. An improved method was first introduced to achieve this target, in which a 3D finite element model for the soil-tunnel system should be established to obtain the overall performance response under excitations of different input waves. The circumferential anchor joint was simulated using the multidirectional springs, while the longitudinal bolt joint was replaced by the beam. Based on the joint opening and offset obtained from the integral model, a refined model of the anchor joint was then set up to further examine its mechanical behavior under the seismic action. The responses of deformation and stress were finally discussed to interpret the safety status of the longitudinal and circumferential joints. The method developed in this paper can also be accessed to seismic response analysis of other types of new joints with complicated structures in shield tunnels.

## 2. Project Overview

A metro line has a total length of approximately 11 km, in which the shield tunneling is adopted to construct the underground section. The design working life of the metro tunnel is 100 years, while the corresponding seismic precautionary intensity is 8-degree. There are nine stations in total. According to the design data, the shield tunnel is approximately 6.7 km in length, and has a maximum buried depth of 28 m from the ground to the roof of the tunnel. Soft soil is widely distributed along the tunnel, while sandy clay, silt, and silty sand can also be found. During the construction, the shield tunnel successively passes through silt sand, sandy clay, muddy clay, fine-silty sand, and clay, whose depths are listed in Section 4.1.2. The ground elevation is 2 m–3 m. The water level is 2 m below the ground surface, implying that the maximum water table can reach 26 m. The metro tunnel is constructed as a new transport line in the suburbs, and there are no other projects in the near vicinity.

The outer diameter, inner diameter, thickness, and width of the segmental lining are 6.6 m, 5.9 m, 0.35 m, and 1.5 m, respectively. Additionally, the universal wedge segment is selected for the assembly of the segmental lining. Each ring has six segments in total, including one K block, two adjacent blocks, and three standard blocks. Different types of joints are adopted for the connections in longitudinal and circumferential directions. M30 bending bolts are selected to connect the adjacent two single segments in the longitudinal joints, while the anchor joint is used for the circumferential joint to make the assembly construction more efficient. There are sixteen anchor joints and twelve bending bolts needed in each ring. The overall view of the cross-section, 3D view, and joints are illustrated in Figures 1–3, respectively.

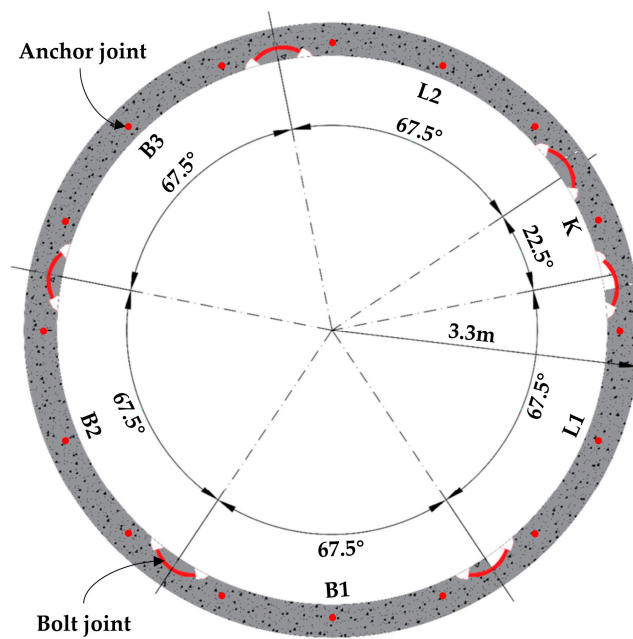


Figure 1. Cross section of the shield tunnel.

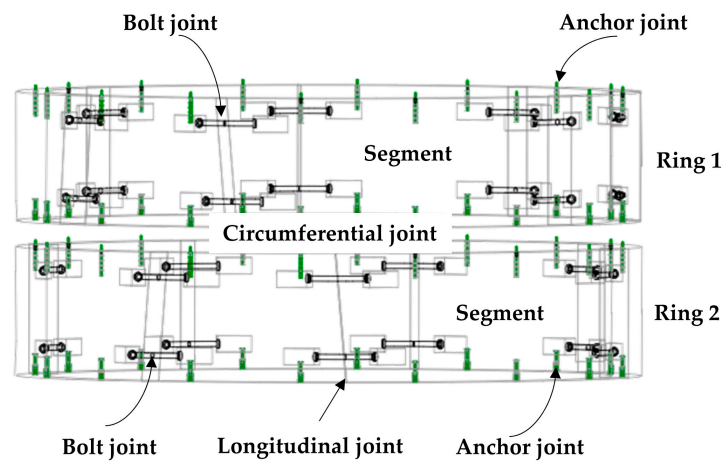


Figure 2. 3D perspective scene of the segmental lining and joints.

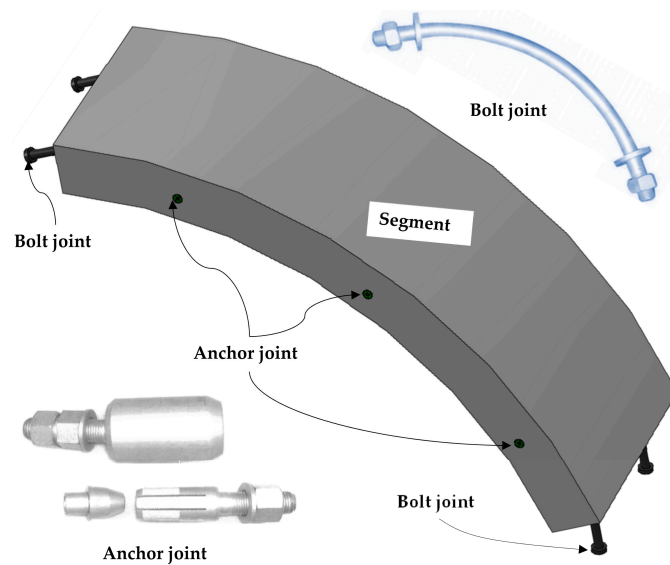
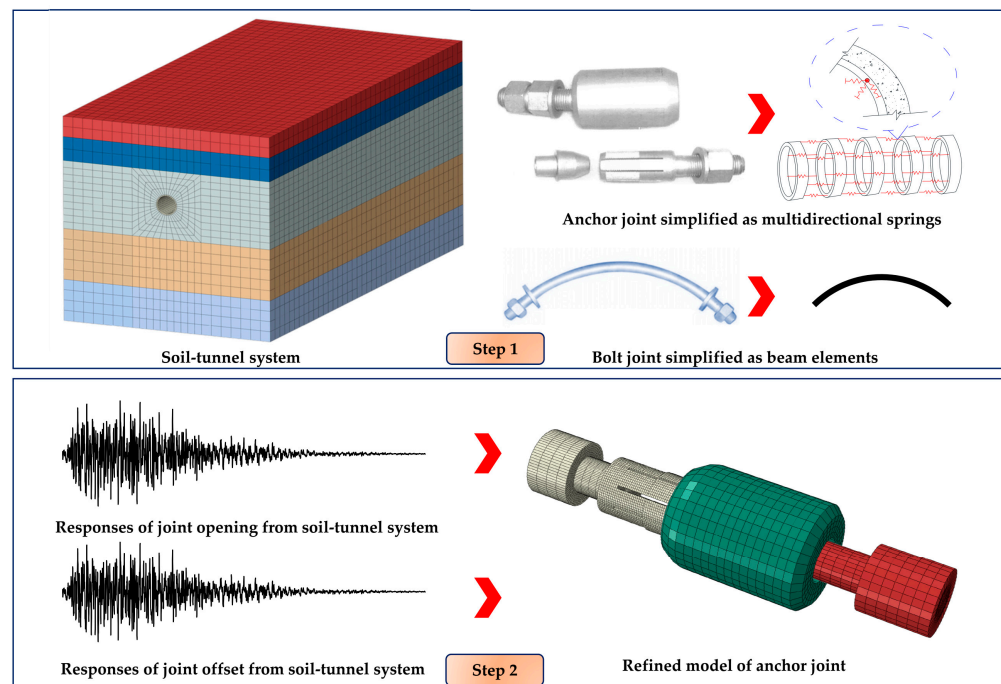


Figure 3. Local details of the segment and joints.

### 3. Improved Method to Investigate Seismic Response of Anchor Joint

An improved method is proposed and introduced in this section to conduct the seismic response of anchor joint in shield tunnel considering both the SSI effect and the complicated structural features. Using this method, the whole procedure of the seismic analysis is actually divided into two parts. Firstly, a 3D numerical model should be established for the soil-tunnel system, as shown in Figure 4. This soil-tunnel system contains three-dimensional soil and tunnel models as well as joints. Specifically, the anchor joint and bolt joint are simplified as the springs and beam elements. Therefore, both the soil and structure have been included in the established model for considering the SSI effect. In this way, the SSI effect can be taken into account in this step, and a relatively satisfactory result can be obtained with the computation cost in an acceptable range.



**Figure 4.** Procedure of the improved method.

Then, the joint opening and offset results can be gained from the integral model mentioned above. After that, a refined numerical model will be set up for the anchor joint, which can totally reproduce its structural characteristics. Combing the refined model of the anchor joint with the obtained joint opening and offset results from the integral model, a more detailed exploration can be conducted on the anchor joint.

## 4. Numerical Model and Materials

### 4.1. Soil-Tunnel System

#### 4.1.1. Soil-Tunnel Model

A 3D numerical model was firstly established for the soil-tunnel system to include the dynamic SSI effect under seismic excitations in ABAQUS. The length, depth, and width of the model are 120 m, 60 m, and 100 m, respectively. The soil is regarded as the multilayered media, while the tunnel is composed of equivalent areas without joints and key areas with more details. The numerical model and the corresponding mesh results are shown in Figure 5. In this model, the solid C3D8 element is selected for the segment and soil, while the 3D beam element B31 is used to simulate the bending bolt joint. Shear and normal springs are utilized to replace the connection effect of the anchor joint at the same locations with those in practice. The density of mesh for the whole soil-tunnel system model was determined based on [33].

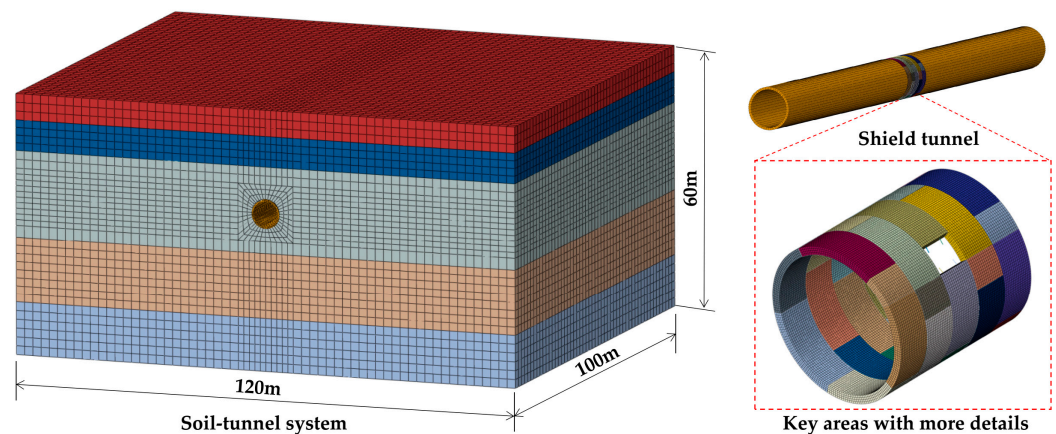


**Figure 5.** 3D numerical model of the soil-tunnel system and local details.

It should be noted that there are five segmental lining rings in the key areas in total, which are connected by bolt joints and anchor joints in the longitudinal and circumferential directions, respectively. In addition, the reduction effect of the segmental joint on the structural stiffness should be considered for the equivalent areas of the tunnel model. In this regard, the equivalent parameter  $\eta$  is introduced to represent the reduction of the flexural rigidity for the lining structures. In this paper, the  $\eta$  is set to be 0.077 on the basis of the published data from [33].

#### 4.1.2. Material Properties

During the calculations, the concrete damage plasticity (CDP) model is adopted to describe the irreparable damage of the concrete under the seismic action. Based on the CDP model, the damage factor ranges from 0 to 1, representing no damage and complete failure of concrete, respectively. As C60 high performance concrete is used for the segmental lining, the corresponding elasticity modulus, Poisson's ratio, shear expansion angle, flow potential offset value, density, cohesion coefficient, and eccentricity are  $3.55 \times 10^4$  MPa, 0.2, 0.67, 2450 kg/m<sup>3</sup>, 35°, 0.001, and 0.1, respectively. Additionally, the ratio of biaxial ultimate compressive strength to uniaxial ultimate compressive strength is set to be 1.16. All the above parameters were determined as Wang et al. reported [41]. More detailed governing parameters of the CDP model for C60 concrete are listed in Table 1. The damage parameters of the concrete can be obtained by the following equation.

$$d_k = \frac{(1 - \beta)\epsilon_k^{\text{in}} E_0}{\sigma_k + (1 - \beta)\epsilon_k^{\text{in}} E_0}, (k = t, c) \quad (1)$$

in which,  $d_k$  denotes the damage parameter, while  $k = t$  means tension and  $k = c$  means compression;  $E_0$  is the initial elasticity modulus of the concrete;  $\epsilon_k^{\text{in}}$  is the strain in the inelastic stage;  $\sigma_k$  is the stress;  $\beta$  is the proportional coefficient of plastic strain to inelastic strain.

On the other hand, the elastoplastic model is employed to describe the plastic behavior of the bending bolt joint. For the bending bolt with a strength grade of 8.8, the corresponding elastic modulus, yield stress, and Poisson's ratio are set to be 210 GPa, 640 MPa, and 0.25, respectively [40]. While for the anchor joint, multidirectional springs with bilinear behavior are used, including the tensile stiffness and shear stiffness. This assumption was used in this paper based on the reports published in [42]. The initial tensile stiffness of the anchor joint is set to be 350 MN/m, while that will be decreased to 0 if the joint opening exceeds 1.5 mm. Similarly, the initial shear stiffness of the anchor joint is 80 MN/m, while that will be increased to 230 MN/m if the joint offset exceeds 2 mm.

**Table 1.** Governing parameters of the CDP model for C60 concrete.

Uniaxial Compressive Stress/(MPa)	Uniaxial Inelastic Compressive Strain	Compressive Damage $d_c$	Uniaxial Tensile Stress/(MPa)	Uniaxial Cracking Tensile Strain	Tensile Damage $d_t$
7.239	0	0	2.720	0	0
22.122	$6.77 \times 10^{-5}$	0.032	2.216	$8.28 \times 10^{-5}$	0.293
32.149	$2.25 \times 10^{-4}$	0.112	1.682	$1.33 \times 10^{-4}$	0.447
34.258	$7.68 \times 10^{-4}$	0.241	1.426	$1.72 \times 10^{-4}$	0.579
29.164	$1.23 \times 10^{-3}$	0.447	1.218	$2.26 \times 10^{-4}$	0.652
23.297	$2.51 \times 10^{-3}$	0.622	0.982	$2.58 \times 10^{-4}$	0.742
19.332	$3.56 \times 10^{-3}$	0.741	0.872	$2.93 \times 10^{-4}$	0.791
14.265	$4.12 \times 10^{-3}$	0.823	0.783	$3.24 \times 10^{-4}$	0.824
11.173	$4.83 \times 10^{-3}$	0.872	0.691	$3.63 \times 10^{-4}$	0.857
10.293	$5.63 \times 10^{-3}$	0.894	0.635	$3.94 \times 10^{-4}$	0.872
8.973	$6.58 \times 10^{-3}$	0.928	0.593	$4.32 \times 10^{-4}$	0.894
7.254	$7.24 \times 10^{-3}$	0.933	0.551	$4.69 \times 10^{-4}$	0.912
4.982	$8.73 \times 10^{-3}$	0.973	0.514	$4.92 \times 10^{-4}$	0.939

During the calculations of wave propagation in soft soil and rock, it is important to capture the soil nonlinearity. Consequently, the equivalent linear approach is selected to define the approximate nonlinear behavior of soil through a continuous update of the shear modulus and damping ratio according to the calculated soil strain, which has been widely used in this field. The maximum shear modulus of the soil can be calculated from the following equation. More detailed geological properties of different soil layers can be found in Table 2.

$$G_{\max} = \rho V_s^2 \quad (2)$$

where,  $G_{\max}$  is the maximum shear modulus;  $\rho$  is the density;  $V_s$  is the shear wave velocity.

**Table 2.** Properties of the soil layers.

Layer	Density/( $\text{kg/m}^3$ )	Shear Wave Velocity/(m/s)	Poisson's Ratio	Friction Angle/( $^\circ$ )	Cohesion/(kPa)
Slit	1720	180	0.45	36	10
Clay	1780	220	0.32	32	18
Silty clay	1840	270	0.38	30	26
Sand	1950	340	0.25	40	2
Bedrock	1920	600	0.20	-	-

#### 4.1.3. Contact Relationships

As there are lots of different components in the soil-tunnel system, it is of significance to select the correct contact relationships to describe the interaction between them. The surface-to-surface contact in ABAQUS is employed to simulate the interaction between the soil and the segmental lining structures, while the bolt joint is embedded in the segmental linings. Moreover, the hard contact is set for the normal behavior of the surface-to-surface contact, and the penalty friction approach is used with finite sliding formulation in the tangential direction. The friction coefficient between the soil and segments is 0.5, while that between different segments is set to be 0.55.

#### 4.1.4. Boundary Conditions

Since the numerical model of the soil-tunnel system only has a limited range of soil instead of the practical infinite space, it is essential to include an artificial boundary to make sure that the scattering waves can be eliminated on the boundary. In this paper, the viscous-spring boundary proposed by Gu et al. [43] is adopted, whose efficiency has been greatly verified in many publications [44,45]. When using the viscous-spring boundary, a

great number of springs and dampers should be added on the boundary nodes. For each boundary node, the viscous-spring boundary is shown as Figure 6.

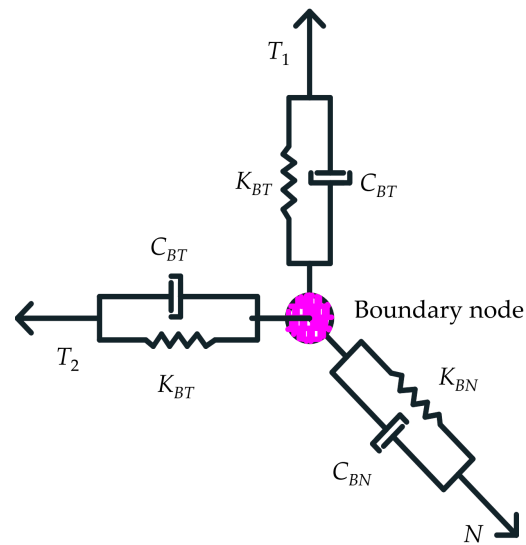


**Figure 6.** Viscous-spring boundary.

The coefficients of the springs and dampers can be obtained from the following equations:

$$K_{BT} = \alpha_T G / r, \quad K_{BN} = \alpha_N G / r \quad (3)$$

$$C_{BT} = \rho c_s, \quad C_{BN} = \rho c_p \quad (4)$$

where,  $K_{BT}$  and  $K_{BN}$  are the spring coefficients in the two different directions, respectively;  $C_{BT}$  and  $C_{BN}$  are the damping coefficients in the two different directions, respectively;  $\alpha_T$  and  $\alpha_N$  are modified coefficients for the spring coefficients;  $r$  is the distance from calculated nodes to the input wave;  $G$  is the soil shear modulus;  $c_s$  is the velocity of shear wave, while  $c_p$  is the velocity of the P wave.

#### 4.1.5. Earthquake Records

Two seismic waves are selected in this paper to conduct dynamic analysis on soil-tunnel system, defined as wave 1 and wave 2, respectively. The acceleration time histories of the two used seismic waves are displayed in Figure 7. According to the design requirements of the shield tunnel, the amplitude of 0.15 g is set for the two seismic waves with the exceedance probability of 10% in 50 years.

Additionally, as the tunnel has a much greater length than its diameter, the seismic behavior of the tunnel may show obvious difference when subjected to the earthquake from different directions. To take into account the possible influence caused by the incident direction of the seismic waves, three different cases are included, including the earthquake motion along the axial direction of tunnel, along the transverse direction of tunnel, and the two-directional horizontal earthquake. For the two-directional horizontal earthquake conditions, the ratio of transverse acceleration amplitude to axial acceleration amplitude is set to be 1:0.85. Hence, there are six cases in total designed for the seismic responses analysis, which is listed in Table 3.

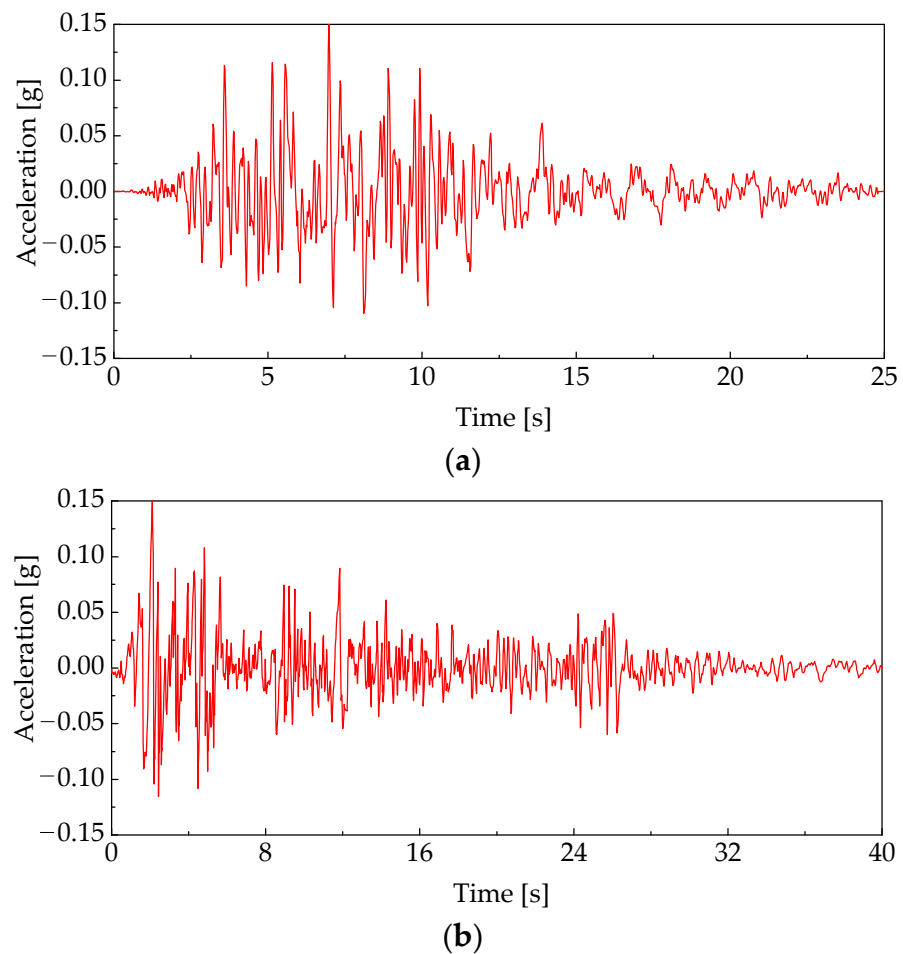


**Figure 7.** Acceleration time histories of seismic waves. (a) Wave 1. (b) Wave 2.

**Table 3.** Cases for seismic response analysis.

Case No.	Incident Direction	Transverse Direction	Peak Acceleration	Axial Direction	Peak Acceleration
1	Transverse	Wave 1	0.15 g	-	-
2	Axial	-	-	Wave 1	0.15 g
3	Two-directional	Wave 1	0.15 g	Wave 1	0.1275 g
4	Transverse	Wave 2	0.15 g	-	-
5	Axial	-	-	Wave 2	0.15 g
6	Two-directional	Wave 2	0.15 g	Wave 2	0.1275 g

#### 4.2. Refined Model of Anchor Joint

##### 4.2.1. Refined Numerical Model of Anchor Joint

Figure 8 shows the 3D refined numerical model and mesh of anchor joint, and two segments are also included in this model. Each segment has a width of 0.75 m, a center angle of 22.5°, and the same thickness with that in the soil-tunnel system. The detailed dimensions of the anchor joint can be found in [40]. The solid C3D8 element is employed to simulate both the anchor joint and segment, and finer mesh is used for the anchor joint as well as the adjacent contact areas for reliable accuracy.

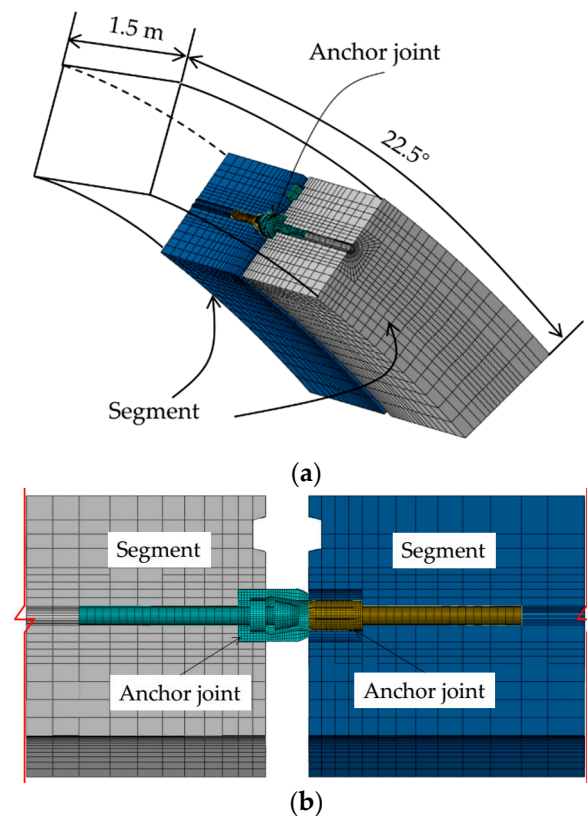


**Figure 8.** Refined numerical model of anchor joint. (a) 3D view. (b) Plan view.

From Figure 8, it can be seen that the anchor joint herein consists of three components, i.e., rod, lantern ring, and sleeve. During the construction of the shield tunnel with the anchor joint, the circumferential joint can be directly connected without extra manual operation due to the automatic self-join of the anchor joint. Under the pressure of jack, the rod will be inserted into the sleeve, while the six sleeve walls will further deform to fill the gap between the rod and lantern ring. Based on the above linkage mechanism, the assembly of anchor joint will be completed, which provides high tensile strength.

#### 4.2.2. Material Properties

The CDP constitutive model is used for the two segments, and the corresponding parameters are totally identical to those listed in Section 4.1.2. The elastoplastic constitutive model is adopted for all of the components in the anchor joint. The elasticity modulus of the anchor joint is 181 GPa, while the yield stress is 530 MPa. The Poisson's ratio is 0.26.

#### 4.2.3. Contact Relationships

Given that the anchor joint is actually embedded during the fabrication of the concrete segment in practice, the anchorage zone of the joint is tied with its adjacent concrete, whereas the surface-to-surface contact formulation is employed for the other integrations. The penalty coefficient of interface between anchor joint and concrete is set to be 0.25, while that between different components of the anchor joint is 0.5 to reproduce the fastening effect according to [40].

#### 4.2.4. Boundary and Loading Conditions

Since the refined model is loaded using the obtained joint deformation from the soil-tunnel system, an appropriate boundary condition should be used to simulate the same situation with that in the integral model. For this purpose, the following boundary condition is introduced as shown in Figure 9. That is, the three surfaces of the right segment are set as the constrained boundary, while no constraints exist for the other components.

With such boundary conditions, the loading procedure of the refined model can be divided into two steps. In step 1, the assembly of anchor joint is completed by pushing the left concrete. After that, the joint offset and opening can be loaded on the anchor joint by applying the obtained deformation.

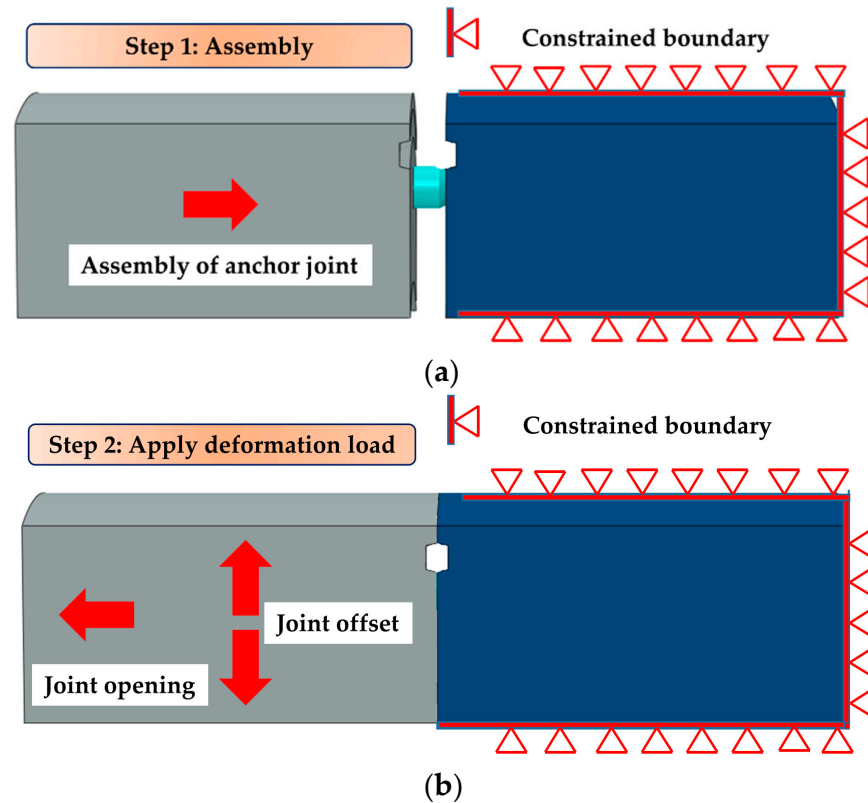


**Figure 9.** Boundary and loading conditions. (a) Step 1. (b) Step 2.

#### 4.3. Model Validation and Convergence Study

In this section, to validate the effectiveness and reliability of the refined numerical model of the anchor joint, a comparison study is conducted on the mechanical behavior of the anchor joint during the assembly and tension deformation. Specifically, the results obtained from the model shown in Figure 8 are calibrated against those recorded in the tests conducted by Shirato et al. [38]. In their tests, a single anchor joint was used, and the reinforced concrete segment was simulated by the metal bases. During the tests, the anchor joint was first assembled. After that, the tensile load was imposed on the assembled anchor joint to investigate its tensile performance. For the verification analysis, the anchor joint is first in a separate state as shown in Figure 9a. Then, the anchor joint will be assembled with a thrust action, illustrated in Figure 9b, which are totally the same with those in tests. In the process mentioned above, a displacement-force curve can be drawn. Similarly, another relationship between the displacement and force can be gained during the tension deformation.

Meanwhile, a convergence study is also necessary to determine the reasonable mesh size according to the corresponding accuracy of the models with different mesh results, so that a good balance can be reached between the computational cost and precision. Looking at this target, three models with small mesh size, medium mesh size, and large mesh size are established for comparison. The experimental and numerical results during the assembly and tension deformation of the anchor joint are shown in Figure 10.

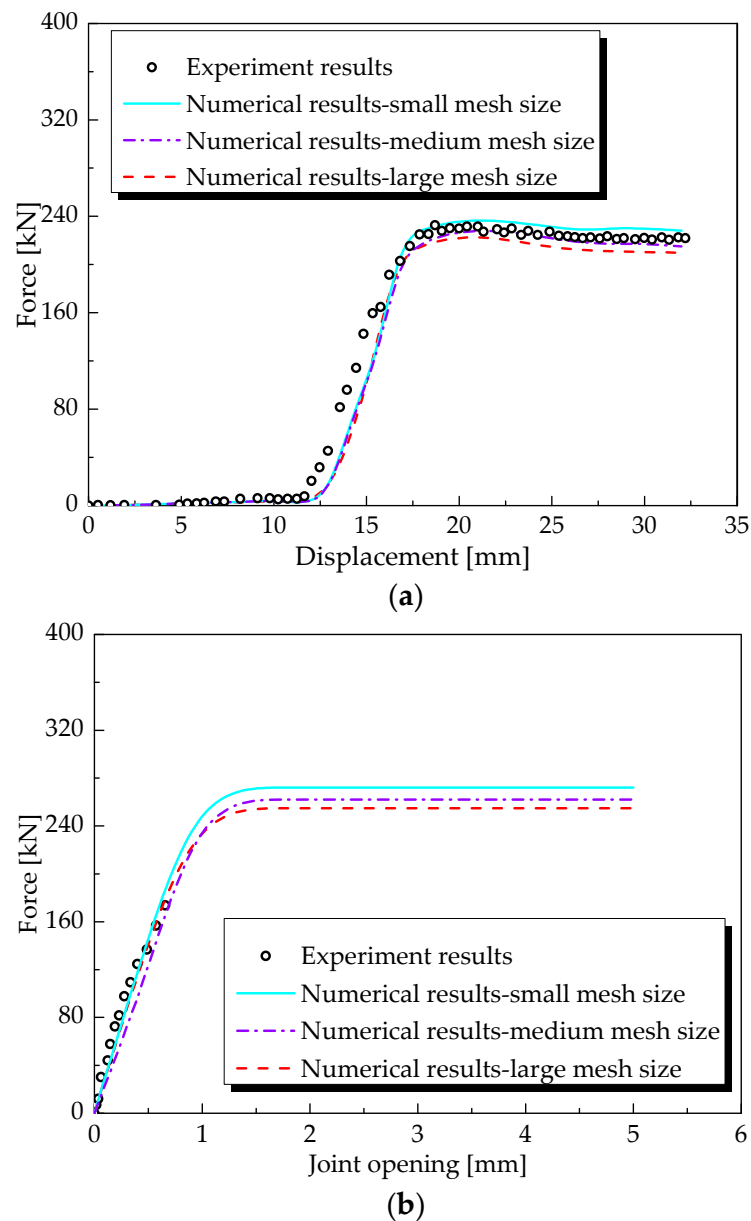


**Figure 10.** Comparison between experimental and numerical solutions. (a) Displacement-force curve during assembly process. (b) Joint opening-force curve during tension deformation process.

During the convergence study, the small mesh size has a basic dimension of 1 mm for the rot and sleeve, while that for the lantern ring is 3 mm. The medium mesh size has a basic dimension of 3 mm for the rot and sleeve, while that for the lantern ring is 5 mm. For the large mesh size, the basic dimensions of the rot, sleeve, and lantern ring are 5 mm, 5 mm, and 8 mm. As the concrete segment is not the main component in the model, its mesh size remains unchanged during the convergence study. From Figure 10, it can be found that the numerical results agree well with the experiment results in both the assembly and tension deformation process, whichever mesh size is adopted. The comparison between experimental and numerical solutions provides evidence that the numerical model has the satisfactory reliability. Thus, all of the three examined mesh sizes can be used for further study of the mechanical behavior of the anchor joint. Since using the medium mesh size shows the best computational efficiency according to the calculation process, the medium mesh size is finally employed in the subsequent analysis.

### 5. Seismic Response of Anchor Joint

#### 5.1. Joint Opening and Offset

The deformation of four circumferential joints in the key areas of tunnel model are shown in Figures 11 and 12. When the seismic wave is input from the transverse directions, the maximum joint opening is found at tunnel arch waist, while the minimum value is at the arch bottom. For the axial seismic conditions, the maximum joint opening is found at arch bottom or the arch vault of the tunnel, while the minimum value is at the arch waist. Besides, it can be seen that these four circumferential joints show similar joint opening distribution behavior, although the detailed values are slightly different. However, this is not true for the two-directional conditions, in which obviously distinct joint deformation can be observed for different joints.

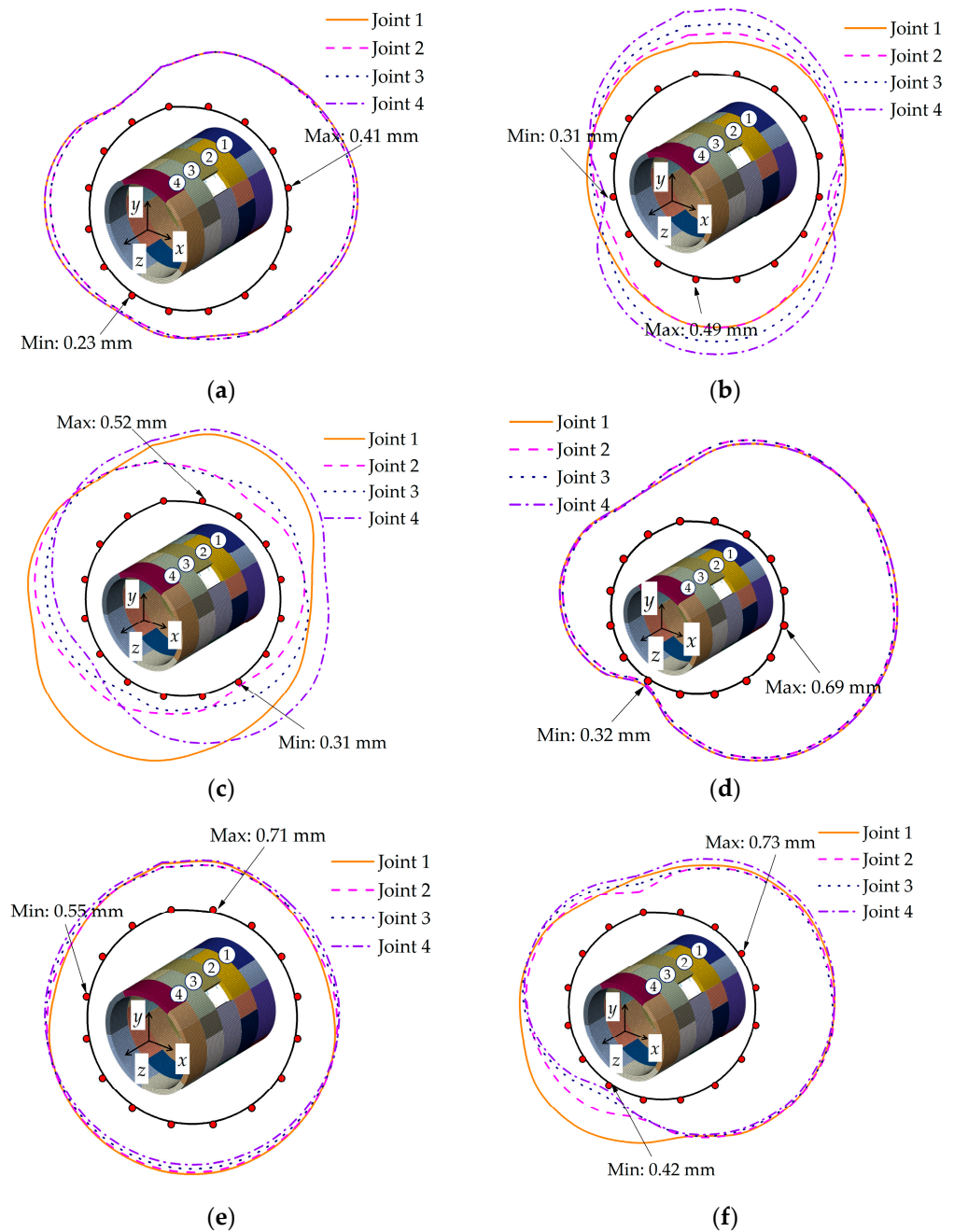


**Figure 11.** Maximum circumferential joint opening. (a) Case1. (b) Case2. (c) Case3. (d) Case4. (e) Case5. (f) Case6.

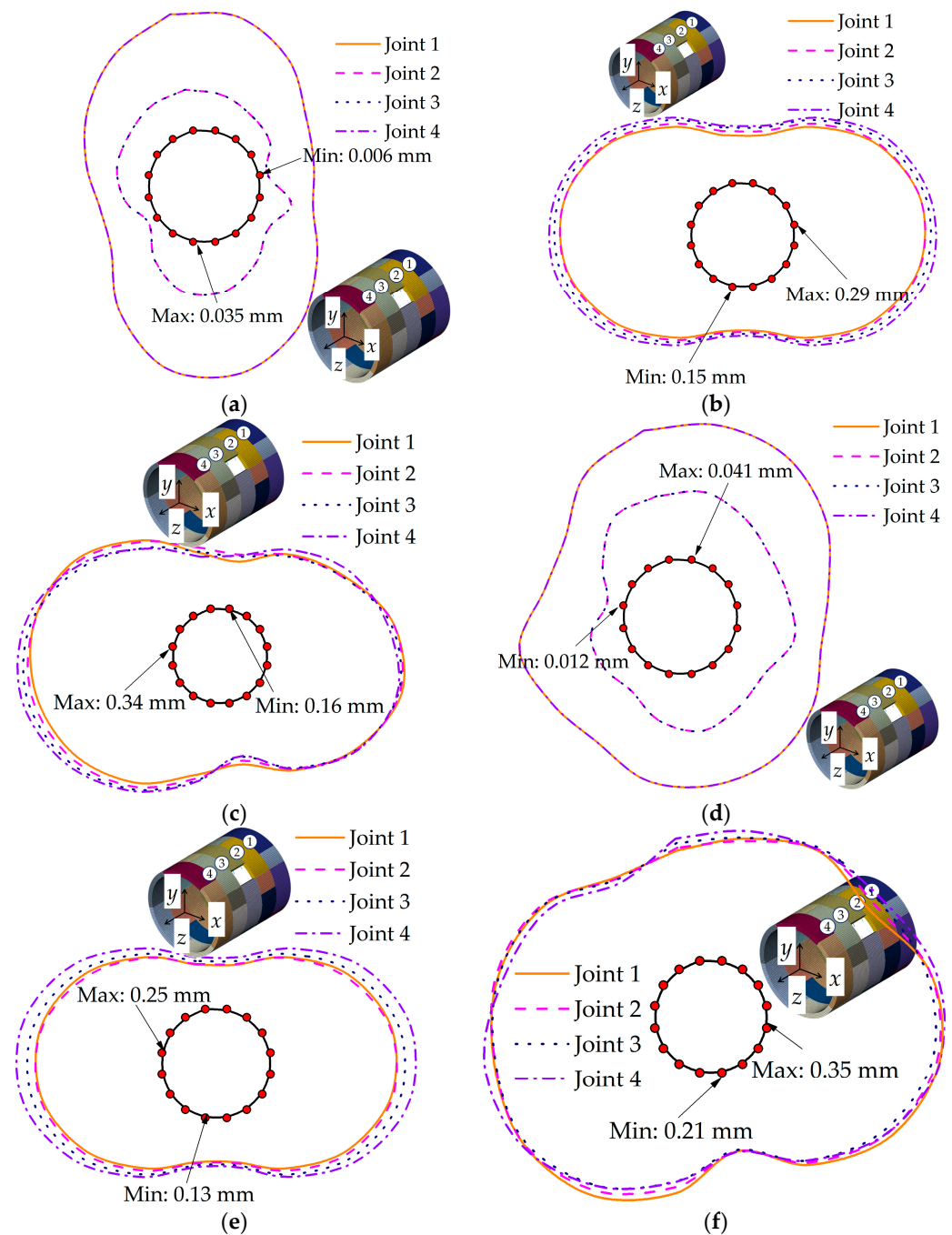


**Figure 12.** Maximum circumferential joint offset. (a) Case1. (b) Case2. (c) Case3. (d) Case4. (e) Case5. (f) Case6.

Moreover, the maximum circumferential joint opening is 0.41 mm, 0.49 mm, 0.52 mm, 0.69 mm, 0.71 mm, and 0.73 mm in cases 1–6, respectively, which are generally larger than the longitudinal joint opening. According to this finding, the circumferential joint may be vulnerable to larger deformation than the longitudinal joint under the same earthquake motion. Additionally, it is worth noting that the joint opening under the two-directional excitations is a little bit greater than the unidirectional conditions. Though there is only a small increasing level, the amplified effect caused by the two-directional excitations cannot be neglected for the sake of safety evaluations.

Figure 12 shows the envelope curves of the circumferential joint offset results. From Figure 12, apparent distribution characteristics can be found under different seismic conditions. For the transverse excitations, the maximum joint offset locates at the arch bottom

and arch vault of the tunnel, while the minimum value is at the tunnel arch waist. For the axial excitations, the maximum joint offset is found at the tunnel arch waist, whereas the minimum one is at the arch bottom and arch vault, which is just opposite to that of the maximum value. Moreover, the joint offset under the transverse excitations is much smaller than that under the axial excitations. Take the wave 1 for example, according to the comparison of case 1 and case 2, the maximum joint offset grows from 0.035 mm to 0.15 mm by increasing nearly 500 percent. In addition, the distribution of the offset under two-directional excitations is similar to that of the axial conditions. This is because the transverse seismic wave has almost no influence on the circumferential joint offset, as the joint offset under the transverse excitations is too small to be considered. The maximum circumferential joint offset is 0.29 mm, 0.34 mm, 0.25 mm, and 0.35 mm in the case 2, case 3, case 5, and case 6, which is nearly half of the corresponding joint opening. Combining the longitudinal joint deformation results, it can be primarily drawn that the seismic action leads to more negative impact on the joint opening than the joint offset.

Zhang et al. [33] conducted seismic response analysis of bolt joints in shield tunnels. According to their findings, the maximum circumferential joint opening and offset can reach 0.7 mm and 0.5 mm under transverse excitations with a peak acceleration of 0.1225 g. While under axial excitation conditions, the maximum circumferential joint opening and offset can reach 0.9 mm and 0.6 mm, respectively. Compared with the bolt joint, the deformation of anchor joint subjected to seismic waves with the same amplitude is smaller. This indicates that the anchor joint has a better bearing capacity. Besides, the deformation of bolt joint under axial excitation is larger than that under transverse excitation, which is similar to that found in this paper.

### 5.2. Stress Distribution Characteristics of Anchor Joint

The stress distribution results of the anchor joint on the basis of the refined numerical model are displayed in Figure 13. For easy observation, the symmetrical plane passing through the axis of the anchor joint is selected as the sectional view. Figure 13a shows the stress of the anchor joint after finishing the assembly of rod, sleeve, and lantern ring, which is the perfect working state of the joint. In this case, the maximum stress of the joint is 510 MPa, locating at the sleeve walls. It is obvious that most of the stress concentration areas are on the sleeve walls, implying that the three components of the anchor joint have been firmly connected so that the satisfactory tensile property can be obtained. Additionally, the lantern ring is the main component to bear the large deformation and generate the tightening force. The anchor joint has entered the plastic deformation stage under the normal working conditions, which is quite different from the conventional bolt joints.

After loading the deformation responses of the joint, the maximum stress responses of the anchor joint under the six different selected cases are illustrated in Figure 13b–g. It is found that obvious changes happen on both the maximum stress and its distribution features. Specifically, the maximum stress decreases to 464 MPa, 459 MPa, and 462 MPa under the different input conditions of wave 1, while that for the wave 2 is 451 MPa, 449 MPa, and 447 MPa, respectively. Consequently, the maximum stress of the anchor joint decreases in varying degrees after bearing the seismic load, which is mainly due to the change of the relative position of the segments, leading to the change of the relative position between the rod, sleeve walls, and lantern ring. With the joint deformation, especially for the joint opening, a separation trend of the three components will appear, which finally weakens the integrity of the anchor joint. On the other hand, friction is extremely important to keep the tensile bearing capacity of the anchor joint. The change of the relative position of each component may lead to the decrease of the contact pressure between components and further cause the loss of the bearing capacity of the anchor joint.

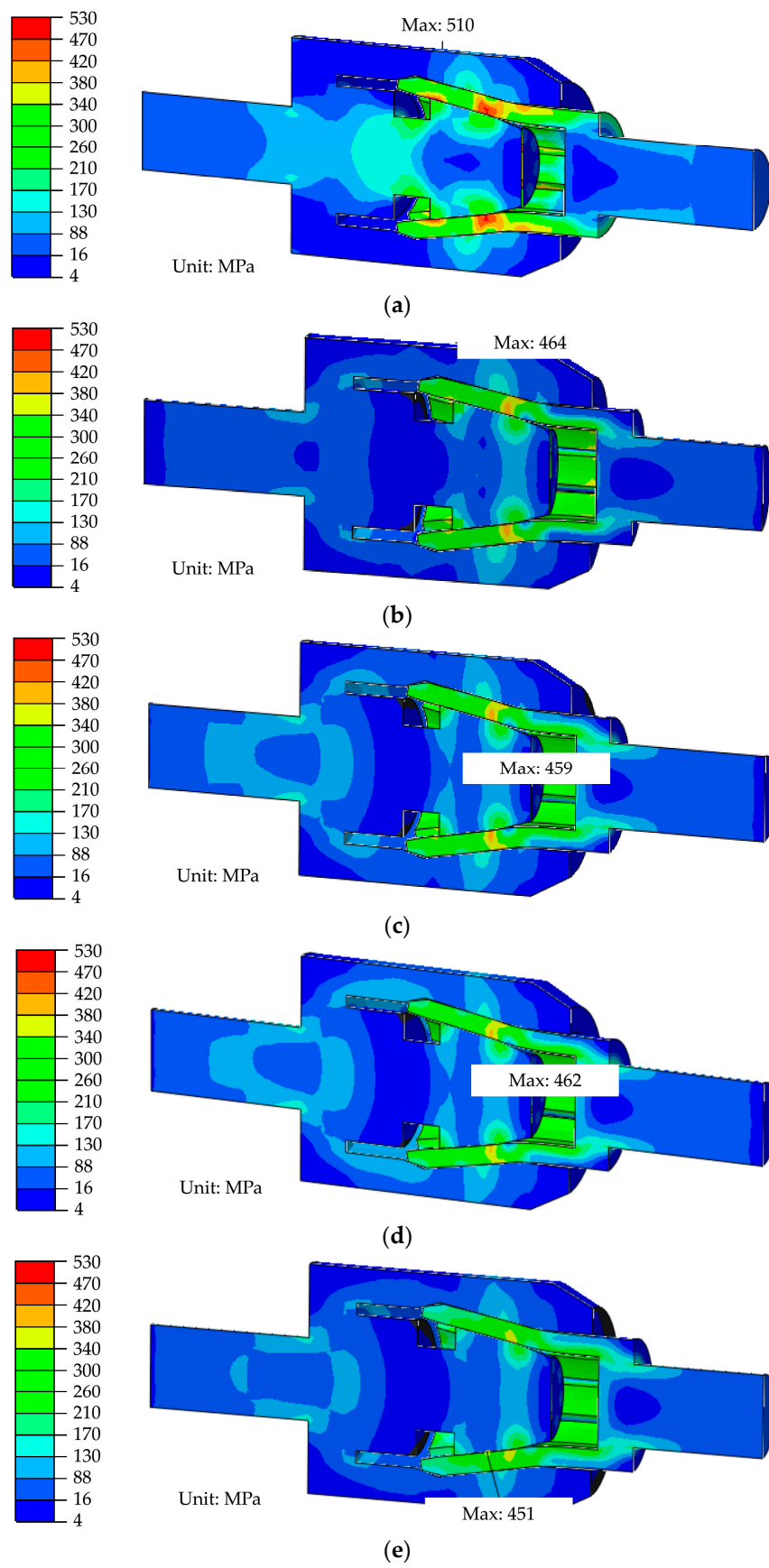
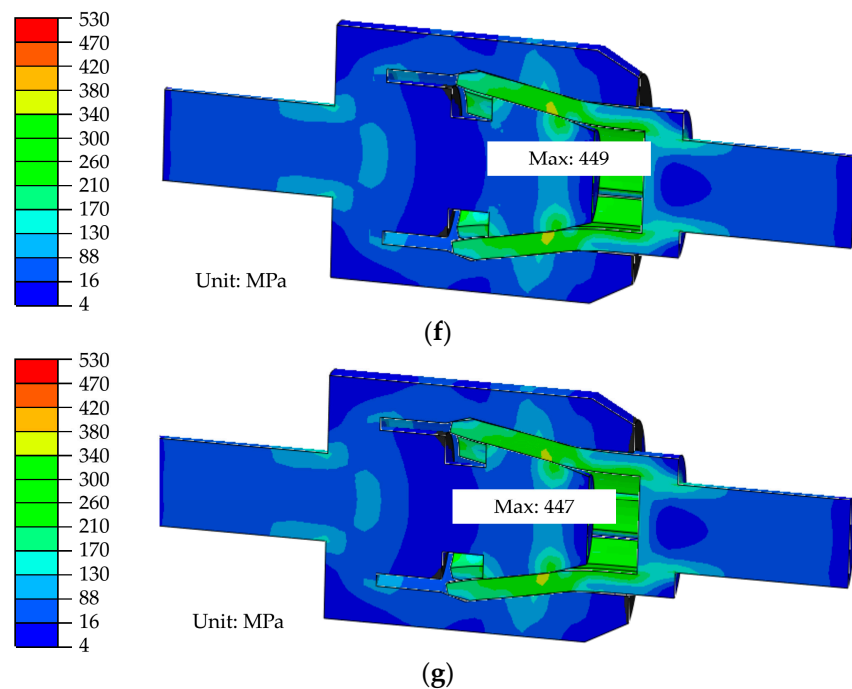


Figure 13. Cont.



**Figure 13.** Stress distribution of anchor joint. (a) After assembly. (b) Case1. (c) Case2. (d) Case3. (e) Case4. (f) Case5. (g) Case6.

In addition, the influence of the structural characteristics of the anchor joint on its seismic response must be fully considered. As the anchor joint is a composite structure, if the components are separated only within a certain range under the action of earthquake, the main impact result is the decline of structural integrity. However, the loss of integrity will not cause irreversible structural damage to a single component, which is essentially different from the traditional bolt joint. The recoverability of anchored joints in a certain range of deformation makes them have better resistance to large deformation loads. Therefore, when analyzing the stress characteristics of anchored joints under earthquake, the final deformation of the joints must be taken into account after the earthquake, in addition to the most unfavorable load combination. According to the maximum joint deformation, it can be judged whether the anchor joint is completely damaged during the earthquake. Meanwhile, the final joint deformation can be used to predict the actual state of the anchor joint after the end of the earthquake load.

### 5.3. Strain Response of Anchor Joint

Based on the stress and deformation results of the anchor joint, the sleeve has the largest deformation among the different components, which play a key role in the bearing capacity of the whole system. Although plastic deformation occurs locally in other components, the value is very small and has little influence on the joint's performance. Therefore, only the main deformation component, namely the sleeve, is analyzed in this section. The plastic strain distribution of the sleeve is shown in Figure 14.

It can be seen from Figure 14a that after the anchor joint is assembled, plastic strain occurs in most areas of the side walls of the sleeve, which is consistent with the stress distribution results. By comparing the plastic strain results at the completion time of assembly and after the application of the most unfavorable seismic displacement responses, it can be found that the plastic strain distribution of the sleeve changes little under the action of different seismic waves, and the maximum plastic strain remains unchanged. It can be inferred that the maximum plastic strain of the side walls of the sleeve occurs at the end of the assembly process. This should happen at the same time with the appearance of the maximum deformation of the sleeve side walls.

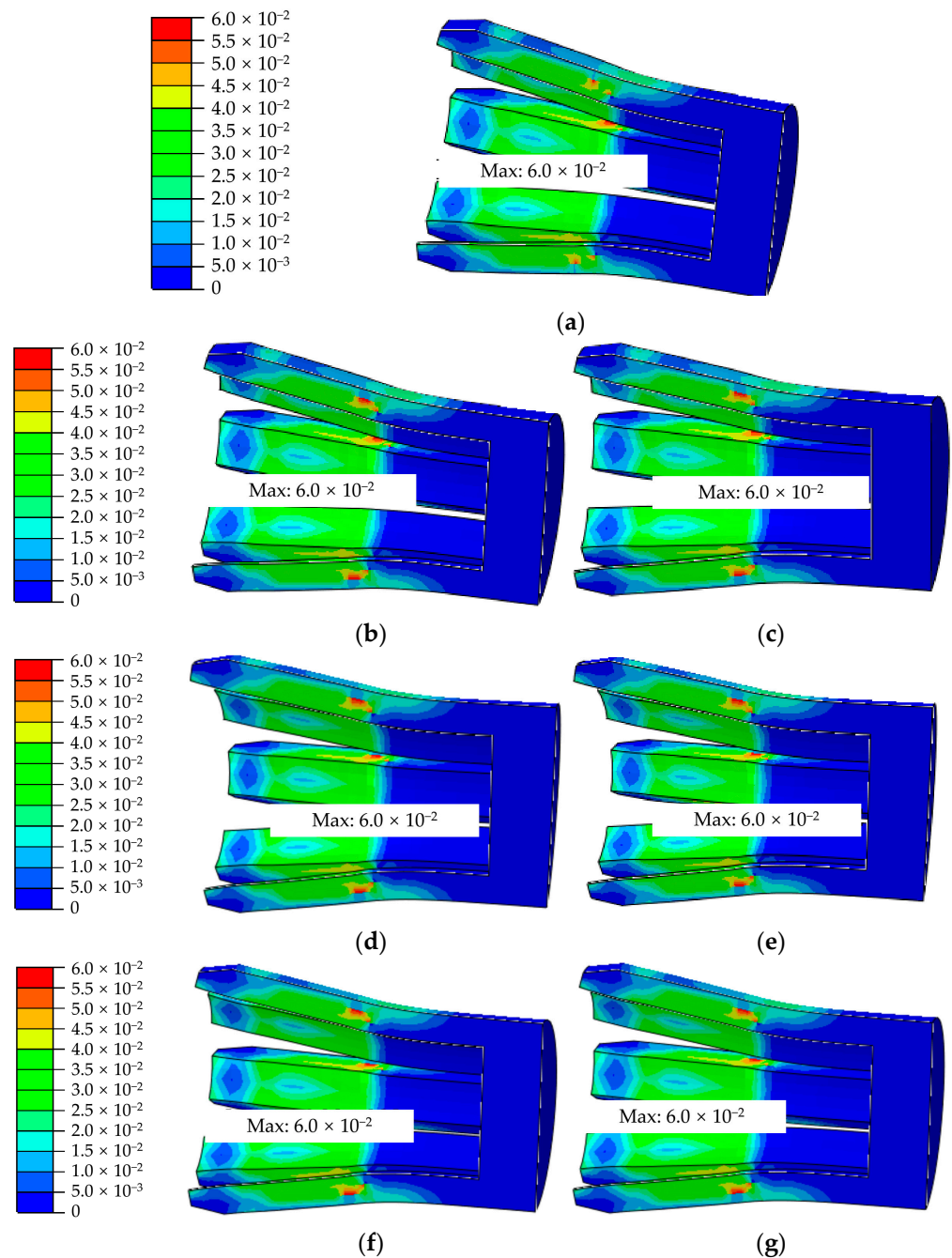


**Figure 14.** Plastic strain of lantern ring. (a) After assembly. (b) Case1. (c) Case2. (d) Case3. (e) Case4. (f) Case5. (g) Case6.

Besides, the mutual position change between the joint members within a certain range will not cause the increase of the maximum plastic strain. However, it is worthy of noting that the distribution range of the maximum plastic strain has expanded in Figure 14b–g, and it changes from the edge of the sleeve side walls to the sleeve center. The above results indicate that although the maximum plastic strain value remains the same, the plastic deformation of the sleeve side walls actually increases after the earthquake. The cumulative effect of plastic strain under seismic action has a negative impact on the mechanical performance of the anchor joint. With the continuous expansion of the distribution range of plastic strain, the recovery level of the bearing capacity of each component in the anchor joint after separation and reassembly is bound to decline. Accordingly, it is of critical importance to conduct a detailed seismic response study on the anchor joint based on

the proposed method in this paper. In this way, the deformation characteristics, bearing capacity, and safety state of the anchor joint can be reasonably evaluated in the light of the cumulative plastic deformation of sleeve walls during the earthquake motion.

In fact, most of the existing seismic response studies on shield tunnels have neglected the detailed structural features of the segmental joints. The most important reason is to simplify the model to gain less computational cost. Another critical reason is that it is really difficult to reach convergence during the complicated three-dimensional numerical simulations with too detailed characteristics of the structures. However, in this section, an apparent cumulative effect of plastic strain has been found for the anchor joint under seismic action. This phenomenon demonstrates that it is quite necessary to propose advanced methods, which can reproduce and reflect the real structural features of the segmental joints. Additionally, it can be inferred that for the segmental joints with complex structural components, more detailed investigations are still in need to gain a comprehensive knowledge of their seismic performance.

## 6. Conclusions

This paper aimed to study the seismic response of the anchor joint in shield tunnel considering the SSI effect. For this purpose, an improved method was first developed and introduced in detail. Then, joint deformation characteristics were discussed based on the results obtained from the soil-tunnel system. Finally, the detailed stress and strain distribution features were interpreted to reveal the seismic performance and evaluate the safety state of the anchor joint. The specific conclusions are as follows:

- (1) Combing the dynamic time history method and the response displacement method, an improved approach is proposed for the overall and detailed seismic response study of the anchor joint. Using this method can effectively reduce the modeling difficulty and computing resource consumption caused by the complex structure of the anchor joint.
- (2) The maximum opening and offset of the anchor joint under the axial seismic input are greater than those under the transverse seismic input. The distribution features of joint opening and offset are obviously different under different seismic excitations. The seismic action leads to a more negative impact on the joint opening than the joint offset.
- (3) Compared with the unidirectional seismic input conditions, the maximum opening and offset of the anchor joint under the bidirectional seismic action are increased. However, the deformation of joints at different locations is rather distinct, which cannot be directly obtained from the sum of results from unidirectional seismic input conditions.
- (4) The opening and offset caused by earthquake can cause the separation of the components in the anchor joint, resulting in the decrease of the contact pressure among the components, and further reduce the bearing capacity of the anchor joint. The stress distribution of the sleeve shows obvious changes, while the distribution range of the maximum plastic strain of the sleeve walls is expanded.
- (5) For the evaluation on the deformation resistance and post-earthquake performance of the anchor joint, the final deformation of the anchor joint and the cumulative plastic strain of the sleeve can be used as the quantitative indicators.

The seismic response of anchor joint has been preliminarily studied with the proposed improved numerical method. In this paper, only the results of joint opening, offset, stress, and strain were considered, while more detailed investigations are still necessary to gain a comprehensive understanding of the seismic performance of anchor joints. The influence of geology conditions and seismic waves should also be taken into account, which will be the further work.

**Author Contributions:** Methodology, formal analysis, software, writing—original draft, G.Z.; conceptualization, funding acquisition, writing—review & editing, W.Z.; software, validation, J.Q.; visualization, R.N.; validation, C.Z. All authors have read and agreed to the published version of the manuscript.

**Funding:** This research was supported by the National Natural Science Foundation of China (Grant No. 51978460), which is gratefully acknowledged.

**Conflicts of Interest:** The authors declare no conflict of interest.

## References

1. Editorial Department of China Journal of Highway and Transport. Review on China's Traffic Tunnel Engineering Research 2022. *China J. Highw. Transp.* **2022**, *35*, 1–40. [[CrossRef](#)]
2. Chen, Z.; Liang, S.; Shen, H.; He, C. Dynamic centrifuge tests on effects of isolation layer and cross-section dimensions on shield tunnels. *Soil Dyn. Earthq. Eng.* **2018**, *109*, 173–187. [[CrossRef](#)]
3. Gong, C.; Wang, Y.; Ding, W.; Lei, M.; Shi, C. Waterproof Performance of Sealing Gasket in Shield Tunnel: A Review. *Appl. Sci.* **2022**, *12*, 4556. [[CrossRef](#)]
4. Zhang, G.; Zhang, W.; Li, H.; Cao, W.; Wang, B.; Guo, W.; Gao, P. Waterproofing behavior of sealing gaskets for circumferential joints in shield tunnels: A full-scale experimental investigation. *Tunn. Undergr. Space Technol.* **2021**, *108*, 103682. [[CrossRef](#)]
5. Zhang, G.; Zhang, W.; Cao, W.; Wang, B.; Lai, T.; Guo, W.; Gao, P. A novel test setup for determining waterproof performance of rubber gaskets used in tunnel segmental joints: Development and application. *Tunn. Undergr. Space Technol.* **2021**, *115*, 104079. [[CrossRef](#)]
6. Wang, W.L.; Wang, T.T.; Su, J.J.; Lin, C.; Seng, C.R.; Huang, T.H. Assessment of damage in mountain tunnels due to the Taiwan Chi-chi earthquake. *Tunn. Undergr. Space Technol.* **2001**, *16*, 133–150. [[CrossRef](#)]
7. Lin, G.; Luo, S.; Ni, J. Damages of Metro Structures Due to Earthquake and Corresponding Treatment Measures. *Mod. Tunn. Technol.* **2009**, *46*, 36–41.
8. Zhang, W.W.; Jin, X.L.; Yang, Z.H. Combined equivalent & multi-scale simulation method for 3-D seismic analysis of large-scale shield tunnel. *Eng. Comput.* **2014**, *31*, 584–620. [[CrossRef](#)]
9. Hashash, Y.M.A.; Hook, J.J.; Schmidt, B.; Yao, J.I.C. Seismic design and analysis of underground structures. *Tunn. Undergr. Space Technol.* **2001**, *16*, 247–293. [[CrossRef](#)]
10. Wang, X.; Jin, X.; Wang, P.; Yang, Z. Parallel Dynamic Analysis of a Large-Scale Water Conveyance Tunnel under Seismic Excitation Using ALE Finite-Element Method. *Appl. Sci.* **2016**, *6*, 36. [[CrossRef](#)]
11. Brandis, A.; Kraus, I.; Petrovič, S. Simplified Numerical Analysis of Soil-Structure Systems Subjected to Monotonically Increasing Lateral Load. *Appl. Sci.* **2021**, *11*, 4219. [[CrossRef](#)]
12. Ma, J.; Han, S.; Gao, X.; Li, D.; Guo, Y.; Liu, Q. Dynamic Lateral Response of the Partially-Embedded Single Piles in Layered Soil. *Appl. Sci.* **2022**, *12*, 1504. [[CrossRef](#)]
13. Brachman, R.W.I.; Elshimi, T.M.; Mak, A.C.; Moore, I.D. Testing and Analysis of a Deep-Corrugated Large-Span Box Culvert prior to Burial. *J. Bridge Eng.* **2012**, *17*, 81–88. [[CrossRef](#)]
14. Abdel-Sayed, G.; Salib, S.R. Minimum Depth of Soil Cover above Soil-Steel Bridges. *J. Geotech. Geoenviron.* **2002**, *128*, 672–681. [[CrossRef](#)]
15. Yeau, K.Y.; Sezen, H.; Fox, P.J. Simulation of Behavior of In-Service Metal Culverts. *J. Pipeline Syst. Eng.* **2014**, *5*, 04013016. [[CrossRef](#)]
16. Kasper, T.; Meschke, G. A numerical study of the effect of soil and grout material properties and cover depth in shield tunnelling. *Comput. Geotech.* **2006**, *33*, 234–247. [[CrossRef](#)]
17. Maleska, T.; Beben, D. Behaviour of soil-steel composite bridge with various cover depths under seismic excitation. *Steel Compos. Struct.* **2022**, *42*, 747–764. [[CrossRef](#)]
18. Maleska, T.; Beben, D.; Nowacka, J. Seismic vulnerability of a soil-steel composite tunnel—Norway Tolpinrud Railway Tunnel Case Study. *Tunn. Undergr. Space Technol.* **2021**, *110*, 103808. [[CrossRef](#)]
19. Kuribayashi, E.; Iwasaki, T.; Kawashima, K. Dynamic behaviour of a subsurface tubular structure. *Bull. N. Z. Soc. Earthq.* **1974**, *7*, 200–209. [[CrossRef](#)]
20. Luco, J.E.; de Barros, F.C.P. Seismic response of a cylindrical shell embedded in a layered viscoelastic half-space. I: Formulation. *Earthq. Eng. Struct. D* **1994**, *23*, 553–567. [[CrossRef](#)]
21. De Barros, F.C.P.; Luco, J.E. Seismic response of a cylindrical shell embedded in a layered viscoelastic half-space. II: Validation and numerical results. *Earthq. Eng. Struct. D* **1994**, *23*, 569–580. [[CrossRef](#)]
22. Kouretzis, G.P.; Bouckovalas, G.D.; Gantes, C.J. 3-D shell analysis of cylindrical underground structures under seismic shear (S) wave action. *Soil Dyn. Earthq. Eng.* **2006**, *26*, 909–921. [[CrossRef](#)]
23. Chen, J.; Shi, X.; Li, J. Shaking table test of utility tunnel under non-uniform earthquake wave excitation. *Soil Dyn. Earthq. Eng.* **2010**, *30*, 1400–1416. [[CrossRef](#)]
24. An, J.; Tao, L.; Jiang, L.; Yan, H. A shaking table-based experimental study of seismic response of shield-enlarge-dig type's underground subway station in liquefiable ground. *Soil Dyn. Earthq. Eng.* **2021**, *147*, 106621. [[CrossRef](#)]

25. Wang, Z.Z.; Jiang, Y.J.; Zhu, C.A.; Sun, T.C. Shaking table tests of tunnel linings in progressive states of damage. *Tunn. Undergr. Space Technol.* **2015**, *50*, 109–117. [[CrossRef](#)]
26. Wang, F.; Jiang, X.; Niu, J. The Large-Scale Shaking Table Model Test of the Shallow-Bias Tunnel with a Small Clear Distance. *Geotech. Geol. Eng.* **2017**, *35*, 1093–1110. [[CrossRef](#)]
27. Chen, G.; Ruan, B.; Zhao, K.; Chen, W.; Zhuang, H.; Du, X.; Khoshnevisan, S.; Juang, C.H. Nonlinear Response Characteristics of Undersea Shield Tunnel Subjected to Strong Earthquake Motions. *J. Earthq. Eng.* **2020**, *24*, 351–380. [[CrossRef](#)]
28. Miao, Y.; Yao, E.; Ruan, B.; Zhuang, H. Seismic response of shield tunnel subjected to spatially varying earthquake ground motions. *Tunn. Undergr. Space Technol.* **2018**, *77*, 216–226. [[CrossRef](#)]
29. Amorosi, A.; Boldini, D.; Falcone, G. Numerical prediction of tunnel performance during centrifuge dynamic tests. *Acta Geotech.* **2014**, *9*, 581–586. [[CrossRef](#)]
30. Lee, K.M.; Hou, X.Y.; Ge, X.W.; Tang, Y. An analytical solution for a jointed shield-driven tunnel lining. *Int. J. Numer. Anal. Methods Geomech.* **2001**, *25*, 365–390. [[CrossRef](#)]
31. Zhao, T.; Liu, W.; Ye, Z.; Mosallam, A.S. Effects of Water Inrush from Tunnel Excavation Face on the Deformation and Mechanical Performance of Shield Tunnel Segment Joints. *Adv. Civ. Eng.* **2017**, *2017*, 5913640. [[CrossRef](#)]
32. Jin, H.; Yu, S.; Zhou, S.; Xiao, J. Research on Mechanics of Longitudinal Joint in Shield Tunnel by the Nonlinear Spring Equivalent Method. *KSCE J. Civ. Eng.* **2018**, *23*, 902–913. [[CrossRef](#)]
33. Zhang, W.; Zhang, Q.; Cao, W. Study on Stress and Deformation of Bolt Joints of Shield Tunnel under Static and Seismic Action. *KSCE J. Civ. Eng.* **2021**, *25*, 3146–3159. [[CrossRef](#)]
34. Liu, Y.; Zhang, M.; Li, P.; Wang, B.; Wang, L.; Yuan, P. Experiments on the seismic performance of Y-shape joints of subway stations built by enlarging two parallel shield tunnels. *Tunn. Undergr. Space Technol.* **2021**, *115*, 104048. [[CrossRef](#)]
35. Yang, C.; Mo, H.; Chen, J.; Wang, Y.; Giunta, G.; Guan, Z. Influence of Seismic Loading on Segment Opening of a Shield Tunnel. *Sci. World J.* **2014**, *2014*, 387210. [[CrossRef](#)]
36. Yan, Q.X.; Bao, R.; Chen, H.; Li, B.J.; Chen, W.Y.; Dai, Y.W.; Zhou, H.Y. Dynamic response and waterproof property of tunnel segmental lining subjected to earthquake action. *Earthq. Struct.* **2019**, *17*, 411–424. [[CrossRef](#)]
37. Zhang, W.; Zhang, G.; Lei, H. Research on Shear Performance of FRP-Key Joint for Shield Tunnel and Rationality of Arrangement Based on Plastic-damage Model. *China J. Highw. Transp.* **2017**, *30*, 38–48. [[CrossRef](#)]
38. Shirato, M.; Furuichi, K.; Takimoto, K.; Hara, H.; Mukuno, K.; Yoshida, K. Development of New Composite Segment and Application to the Tunneling Project. *J. JSCE* **2003**, *728*, 157–174. [[CrossRef](#)]
39. Nakajima, S.; Akiyama, S.; Yasaka, M.; Sato, H.; Mukuno, K. Development of the Axial-Slide Ductile Segment. *Tunn. Eng. Res. Rep.* **1998**, *8*, 39–46.
40. Zhang, W.; Zhang, G.; Su, R.; Jin, M. Numerical Study on Influence of Manufacturing Process on Mechanical Properties of Longitudinal Anchor Joint for Shield Tunnel. *Tunn. Constr.* **2016**, *36*, 150–157. [[CrossRef](#)]
41. Wang, R.; Han, L.; Zhao, X.; Rasmussen, K.J.R. Analytical behavior of concrete filled double steel tubular (CFDST) members under lateral impact. *Thin Wall Struct.* **2016**, *101*, 129140. [[CrossRef](#)]
42. Takeuchi, T.; Emori, Y.; Suda, Y.; Koizumi, A. Influence on segments by jack thrust of shield-driven tunneling. *Doboku Gakkai Ronbunshuu F* **2010**, *66*, 599–611. [[CrossRef](#)]
43. Gu, Y.; Liu, J.; Du, Y. 3D consistent viscous-spring artificial boundary and viscous-spring boundary element. *Eng. Mech.* **2007**, *24*, 31–37.
44. Xu, C.; Song, J.; Du, X.; Zhong, Z. A completely explicit finite element method for solving dynamic u-p equations of fluid-saturated porous media. *Soil Dyn. Earthq. Eng.* **2017**, *97*, 364–376. [[CrossRef](#)]
45. Zhang, X.; Far, H. Effects of dynamic soil-structure interaction on seismic behaviour of high-rise buildings. *Bull. Earthq. Eng.* **2022**, *20*, 3443–3467. [[CrossRef](#)]